Journal of Energy Storage 13 (2017) 378–386

Contents lists available at ScienceDirect

Journal of Energy Storage

journal homepage: www.elsevier.com/locate/est

Overcharge and thermal destructive testing of lithium metal oxide and lithium metal phosphate batteries incorporating optical diagnostics

Frank Austin Mier[a,*], Rudy Morales[a], Caralyn A. Coultas-McKenney[a], Michael J. Hargather[a,*], Jason Ostanek[b,1]

[a] New Mexico Tech, Socorro, NM 87801, United States
[b] Naval Surface Warfare Center Philadelphia Division, Philadelphia, PA 19112, United States

ARTICLE INFO

Article history:
Received 30 January 2017
Received in revised form 21 June 2017
Accepted 14 August 2017
Available online xxx

Keywords:
Lithium batteries
Destructive testing
Overcharge
Schlieren imaging

ABSTRACT

Lithium batteries have a tendency to fail violently under adverse conditions leading to the rapid venting of gas. Overcharge, thermal heating, and a combination of the two conditions are applied here to investigate the gas venting process. A test chamber has been constructed with data recordings including chamber pressure and temperature, battery voltage, current, and surface temperature as functions of time throughout the charging and failure processes. High-speed imaging and schlieren flow visualization are used to visualize the gas venting process. A direct comparison between lithium iron phosphate based K2 26650 and lithium nickel manganese cobalt oxide LG 18650 cells is made through a test series of the three failure methods. Failure under thermal, overcharge, and thermal-overcharge conditions are generally similar in terms of the gas venting process, but are observed to have increasingly energetic failures. The thermal-overcharge abuse condition demonstrates an ability to reconnect via internal short circuit even after an initial electrical failure seen as the refusal to accept charge. This reconnection is associated with a secondary, more energetic failure which can produce weak shock pressure waves.

1. Introduction

Lithium batteries provide a high energy density source which has been applied to most portable applications. Such a concentration of stored electrochemical energy generally involves significant risks in the cases of end user abuse, unexpected loading conditions, design flaws, or manufacturing defects. Examples of lithium battery failures including combustion in popular smartphones and commercial airliners have brought much attention to these hazards [1,2]. With popular uses such as personal electronics and electric vehicle transportation, it is important to understand the failures of these components such that risks can be minimized.

Commercially available lithium secondary cells generally contain one or more different protective devices to minimize the risk from inherently hazardous chemistries. Current interrupt devices (CID) protect during overcharge scenarios by physically separating the cathode from the circuit [3]. Positive temperature coefficient (PTC) devices temporarily protect against thermal loading via increasing resistance. Thermal fuses can also provide protection from excess temperature by permanently or temporarily disconnecting the circuit. Many batteries, including the ones tested here, have vents which allow for the release of gases which can build to dangerous pressure levels, leaving the battery permanently damaged. Separator shutdown provides protection by inhibiting ion transport when the temperature within the cell exceeds the melting point of the separator. If the separator further increases in temperature, it can eventually melt causing violent reactions [4].

The most commercially prevalent group of lithium battery chemistries contain layered, lithium metal oxide cathodes. Examples of this group are lithium cobalt oxide (LCO), lithium nickel manganese cobalt oxide (NMC), and lithium nickel cobalt aluminum oxide (NCA). Under overcharge conditions, cathode decomposition results in generation of oxygen gas and lithium ions [5]. Additionally, intercalated lithium within the electrolyte can react resulting in formation of hydrocarbons [6]. The presence of both oxygen and hydrocarbons presents a significant flammability risk. Research has been done to introduce new chemistries which are cost effective, higher energy density, and inherently more safe. Lithium iron phosphate (LFP) has been presented as thermally

* Corresponding authors.
E-mail addresses: frank.mier@student.nmt.edu (F.A. Mier), michael.hargather@nmt.edu (M.J. Hargather).
[1] Current address: Purdue University, West Lafayette, IN 47907, United States.

http://dx.doi.org/10.1016/j.est.2017.08.003
2352-152X/

stable alternative with a more level discharge voltage curve than lithium cobalt oxide, but it performs at somewhat lower voltage [7]. However, vented cell material analyzed from LCO, NMC, and LFP cells contains hydrogen gas which can present safety concerns [8]. An alternative sodium based chemistry (Na_xFePO_4F) has also shown promise which would be cost effective and less hazardous [9].

Modeling and testing of lithium cells show trends and hazards during battery failures. Numerical models have been created for thermal testing of cells and have shown significant improvement in correlations to experimental data with venting considerations under isentropic flow assumptions [10]. Testing inside an adiabatic calorimeter has shown a relationship between time to failure and state of charge (SOC) in thermal testing which provides data on temperature and pressure [11]. Cone calorimetry tests have also shown the relationship between time to failure and SOC while also showing combustion of 18650 format cells [12]. Thermal imaging and high-speed tomography have shown how specific components of cells breakdown and lead to thermal runaway [13].

Measurements of the external flow associated with battery venting are underdeveloped. Incorporation of high-speed schlieren imaging can visualize refractive gradients in gases associated with chemical species and density variation [14]. This experimental technique can also be used to image pressure and shock wave propagation [15] which could cause undesirable pressure-loading on cells adjacent to a failing cell. The test facility presented here integrates imaging with other common measurements such as voltage, current, temperature, and pressure to provide broad measurements throughout the failure process. The ability to test overcharge and thermal failure conditions allows for a variety of test conditions allowing for test of situations otherwise unexplored.

2. Battery test facility

2.1. Test chamber

A laboratory facility was constructed for the testing, containment, and data collection of lithium battery failures. The facility design focused on creating a reusable and modular enclosure for testing, with instrumentation and remote test operation capabilities. The test chamber, along with all associated electrical systems, are mounted on top of an optical table measuring approximately 2 m by 6 m in a room separated from test operators. An annotated image of the laboratory setup is shown in Fig. 1.

The test chamber is a vessel with four viewing windows and seven ports for overcharge wiring, instrumentation, and air lines for post-test chamber purge. The chamber is a single 254 mm square by 762 mm long steel square tube with 9.5 mm wall thickness. Batteries are aligned with the tube allowing for an axial viewing window on the end of the chamber which is 235 mm square. Side windows viewing perpendicularly to the length of battery cells have a viewing area of 152 mm high and 406 mm wide. All windows are constructed from 12.7 mm thick acrylic which are laser cut and can be easily replaced if damaged during testing. Rubber gaskets and a 12.7 mm thick A36 steel frame which is bolted directly to the chamber provide secure mounting and sealing of the windows.

The interior of the containment chamber is coated with an electrical insulator to isolate batteries as the test chamber structure itself is connected to ground. An anodized optical breadboard is secured to the bottom of the vessel to allow for versatile mounting options. An acrylic cover is placed directly on top of the optical breadboard to minimize possible short circuits between the overcharge circuit positive lead in case of separation from the battery during testing.

Ports allow for instrumentation, purge, and overcharge wiring to be placed within the chamber. The locations and uses for all ports are shown in Fig. 1. Instrumentation crossing into the sealed environment within the chamber includes a piezoelectric pressure transducer (PCB Piezotronics Model 102B15) to measure dynamic pressure, a pressure transducer (Wika Model A10) for static pressure, K-type thermocouples for surface (Omega 5TC-GG-K-24-36) and air temperature (Omega KTSS-14E-6). On opposite side walls of the chamber, two ports are fitted with airtight cord grips allowing for the insulated 4/0 gauge wire leads of the overcharge system. The majority of ports located on the test chamber use a gusset plate with a standard bolt pattern and a matching gasket for simplification of maintenance and reconfiguration. An example such is the addition of a 120 V_{AC} line through port used to measure battery surface temperature. This is necessary on thermal and combination testing. Gusset plates all have a central tapped hole for the appropriate instrument, purge tube, or overcharge line. These plates use NPT standard tapered threads to maintain appropriate seal.

The port for the piezoelectric pressure transducer is flush-mounted to the test chamber such that the diaphragm is coplanar with the top wall of the test chamber to accurately measure the dynamic pressure during battery failures. A 1.65 mm recessed area was milled into the top of the chamber and 3/8-24 UNC tapped through hole allowing the pressure transducer to be threaded to the proper depth and held against a rubber gasket.

The purge system consists of an entrance on the top of the chamber directly above the battery cells and an exit located near the bottom of the chamber on a side wall adjacent to one of the end windows. Gusset plates on the ports connect to Swagelok brand tube fittings using 12.7 mm stainless steel tube. Electrically actuated ball valves are connected to the ends of these tubes, so

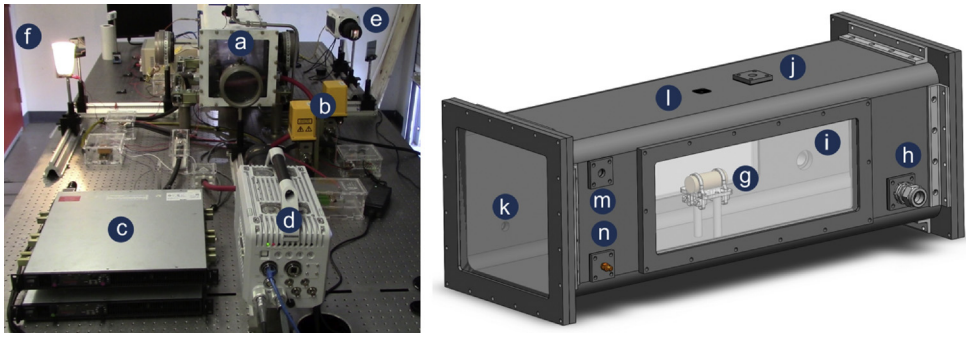

Fig. 1. Left is a photograph of the installed laboratory setup with the (a) test chamber, (b) purge valves, (c) power supplies, (d) axial camera (Photron SA-X2 shown), and (e) side camera (Phantom v711 shown). Test operators are located behind the (f) door. Right is a model of the test chamber with annotated locations for the (g) battery, (h–i) overcharge wiring, (j) purge inlet, (k) purge outlet, (l) piezoelectric pressure transducer, (m) air temperature probe, and (n) surface temperature thermocouple.

both the exit and entrance of the purge can be sealed during testing. The entrance valve connects to a flexible inlet line with compressed air regulated to 210 kPa gauge pressure. The exit valve connects to another flexible hose (6 m long) to an evacuated outdoor space adjacent to the laboratory building. The exit port also has a wire mesh covering to minimize the amount of solid debris forced through the exit valve and into the environment. Additionally, the pressure transducer for measuring static pressure is mounted on the inlet line off of a Tee-junction such that minimal dynamic perturbations will be introduced to the measurement.

2.2. Data acquisition and control

All instrumentation and automated controls are connected to a National Instruments cDAQ system and controlled through LabVIEW. The cDAQ chassis (NI 9188) has cards for measuring analog input 10 V range (NI 9223), analog input 200 mV range (NI 9205), and thermocouples (NI 9212). The 10 V range card is dedicated to the piezoelectric pressure transducer. The 200 mV range card is used to interface with all common ground referenced measurements which include battery voltage, shunt resistor voltage drop (for measuring overcharge current), camera trigger sync, and static pressure. Any of these signals which would normally be outside the range of the card are stepped down through a voltage divider. The cDAQ chassis with cards and associated low amperage wiring are mounted to an acrylic board on the optical table.

Sampling rates are set at 100 Hz, 1 kHz, and 100 kHz for the thermocouples, 200 mV millivolt range card, and the 10 V range card for the piezoelectric pressure transducer, respectively. Data acquisition and file writing are stable at these rates for approximately 30 min of testing.

The data acquisition wiring has undergone optimization to minimize noise. Most signal noise within the system has been minimized through appropriate grounding of all instrumentation and fixtures in the lab to the building. Data lines between the test chamber and control room are also shielded. Noise on all data lines read by the NI 9205 analog voltage card increases during battery failure because of the common ground necessary between the battery and data acquisition card itself. This is minimal on most lines, but is more noticeable on the current measurement from the shunt resistor as this is the smallest magnitude signal being read into the card.

Control operations associated with the physical test sequence of batteries performed via the National Instruments cDAQ system are valve and overcharge operations. Valves are controlled with a relay card (NI 9482) which completes a circuit with a fixed 24 VDC course. This allows independent opening and closing of inlet and exit purge valves. An Ametek XG1700 power supply is used for the overcharge. This power supply has analog programming capabilities which are utilized to control voltage or current depending on the mode selected on the power supply interface. These modes allow an input voltage at small current levels to change the output of the power supplies. An analog voltage output card (NI 9269) from the cDAQ supplies these voltages which then map linearly with the output of the supplies. The 10 VDC output range of the cDAQ card correlated to the full 0 to 84 A output in controlled current mode or 0 to 20 VDC output in controlled current mode.

Manual operations in the laboratory include adjusting the level of power supplied to cartridge heaters and the discharge of voltage within a battery if a failure does not occur. The cartridge heaters used to heat the cells (Omega CSH-102150/120V) use a 120 V_{AC} maximum input. As these resistive heaters will output heat proportional to their electrical power input, a variable autotransformer is used to achieve the desired heat output. Discharge of the batteries is done manually if needed and checked at the end of each test due to the possibility of a total failure of the computer operating the system. Discharge occurs through a bank of three 0.5 Ω high-wattage resistors in parallel. With this, batteries generally discharge at a peak of approximately 22 A which is within safe operating range. Discharge is activated through a disconnect switch in the control room, and monitored though an analog volt meter.

Static pressure measurements were taken during all tests in an attempt to determine the gas volume produced during battery venting. The static pressure measurement is taken in the inlet line on the purge and is located off of a Tee-junction. The static pressure measurement, combined with the chamber temperature and known volume of 40.8 L via the ideal gas law could provide a mass of vented gas. The calculations, however, provided inconclusive measurements due to temperature variations affecting the pressure gage readings, vented gas composition requiring an alteration to the specific gas constant in the ideal gas law, and imperfect sealing of the test chamber. Future work will investigate how to improve the measurement of gas volume vented.

2.3. Optical systems

Schlieren imaging was performed to visualize venting gases from the battery cells during thermal and overcharge testing. Schlieren imaging is a technique of visualizing refractive index gradients in a test region [14]. A parallel-light schlieren system comprised of a point source of light, two matched convex lenses, a vertically oriented knife edge cut-off, and camera is used here. The point source of light is a chip-on-board style LED which is placed at the focal length of the first lens. The light leaving the first lens is thus collimated as it travels into the second lens, creating the test section. The knife-edge cut-off is placed at the focal point of the light after passing through the second lens thus blocking some of the light from entering the camera. Any refractions of light in the test section will be visualized by the camera because light that is refracted will not focus to the same location as the cut-off plane, thus interacting with the knife-edge and creating the light to dark gradients characteristic of schlieren imaging. Fig. 2(a) provides a schematic representation of this technique. Gas density and

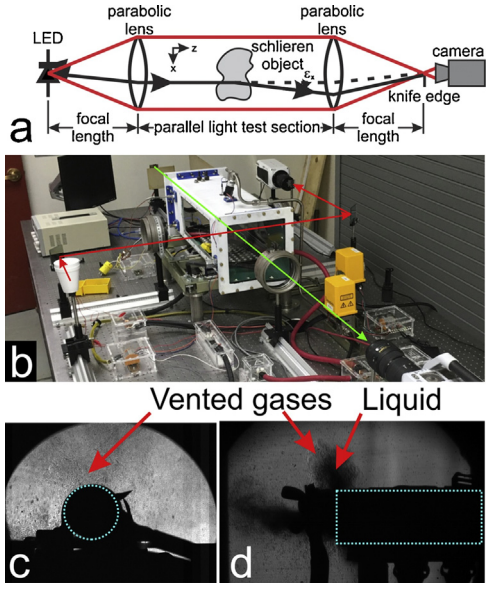

Fig. 2. (a) A schematic representation of the schlieren system used here. (b) Annotated light paths for side (red line) and axial (green line) schlieren with examples of (c) axial and (d) side views of K2 26650 (LFP) cells during tests showing venting of gases and liquid droplets. (For interpretation of the references to color in this figure legend, the reader is referred to the web version of this article.)

chemical species both affect the refractive index of the gas. Thus, any gradients in gas density or species will be visualized. The density gradients visualized included thermal density gradients due to heating, compressible-turbulent flow structures, and pressure waves. In addition to the refractive objects seen in the high-speed schlieren, any solid objects and vented liquids present during the tests are also visualized. Gases and liquids can be distinguished from each other because gases will image as strong light to dark gradients. Comparatively, the liquid electrolyte generally blocks some light thus appearing dark in the image. Dashed cyan lines show the outline of the battery cell in both views in Fig. 2.

Two concurrent axes of schlieren imaging were used to view the battery axially and from the side. The light paths for the axis and side views are seen in Fig. 2(b) alongside example images taken from both perspectives in Fig. 2(c and d). Both arrangements have an approximately 150 mm circular field of view, set by the schlieren lens diameters. The side view schlieren setup is optically folded using first surface mirrors as necessary to fit the system on the optical table.

High-speed images were recorded using a variety of cameras and settings depending on the test conditions. The cameras used included a Photron SA-X2, Photron Mini UX-100, Photron SA-Z (color), and Phantom v711. The high-speed cameras were used for both direct imaging of the batteries and to capture the schlieren images. The direct imaging was particularly useful for tests in which smoke and, ultimately, combustion obscured or reduced the quality of the schlieren images. For all tests with multiple cameras, the cameras were synchronized and provided with a common trigger signal to allow time-correlation between the camera views. The NI data acquisition system recorded the camera trigger time to allow synchronization with the other recorded data.

While schlieren imaging provides utility in visualization of flow structures and is fairly sensitive to changes in refractive index, limitations exist with opacity and chemical species identification. Generally, smoke generation makes schlieren imaging nearly impossible as light transmission is lowered. The only visualized features noted through smoke were combusting, thus light emitting. Schlieren imaging does not provide utility on these tests as the collimated light needed for refractive imaging is mostly blocked. Schlieren imaging visualizes refractive index gradients, which in a single gas system can be directly related to gas density, but in the presence of multiple gas species the density variations cannot be deconvoluted from the species gradients. Thus the schlieren imaging is qualitatively used here to identify the locations of vented gases, but no quantitative density measurement can be made.

3. Comparative testing of lithium metal oxide and lithium metal phosphate cells

3.1. Methods of destructive testing

Three abuse conditions which lead to electrical and physical failures are applied to battery cells mounted in the test chamber: overcharge, thermal, and combined thermal-overcharge loading. Combination tests are explored as they represent a potentially realistic and dangerous situation. These abuse methods involve putting the battery in a charge or environmental state beyond designed operating parameters in which cells will build up high internal temperatures and pressures. Characterized generally by a thermal runaway, internal components of the battery will break down further increasing temperature and pressure conditions within the cell.

Overcharge tests are conducted in a current-controlled power supply operating mode. In this mode, the power supplies regulate output current to a fixed value as long as the battery remains in an closed loop state. In the case of internal battery failures or activation of internal safety mechanisms causing a refusal to accept charge, the power supply will automatically increase, to and hold at, a maximum value of 12 V. Zero current will be measured in the system via the shunt resistor inline with the overcharge as the circuit will be open. The maximum output of the power supply was 84 A, but all tests were conducted at a rate of 10 A. Charging rates were kept much closer to manufacturer specification as initial testing with high charge rates did not provide physical cell failure, only activation of the designed CID.

Dissimilarly, thermal failure tests are controlled manually and heating will continue even after electrical failure of the batteries. Heating is applied via two cartridge heaters described in Section 2.2 which are held to the surface of the cell with hose clamps. A variable autotransformer is used to adjust the heat output of the heaters via changes in voltage. Both cartridge heaters are powered at 60 V_{AC}, corresponding to a 75 W heat generation rate. Individual tests are concluded when visible venting of gases from the cells has ceased, as noted from real-time safety camera video.

Combination tests use both aforementioned abuse sources concurrently. These tests use the same charging and heating rates of the two other abuse conditions so that the battery is experiencing 10 A charge and 75 W external heating. Since the variable autotransformer is separate from the control system for the DC power supplies, the two sources are activated roughly simultaneously. The point when current reaches 10 A is used in analysis as the start of the test.

Battery failures are determined from various operator observations of real time data and imagery based on considerations associated with the failure method being tested. Anticipation of the failures with real time data is a key factor for triggering of high-speed schlieren recordings. Voltage and current measurements can be used as precursors to venting failure as discussed in Section 4.2. Additionally, surface temperature increases on the cell precede the physical failure of cells due to thermal runaway. While data recording remains active for some time after cell failure, all image recordings are performed with a post-trigger using the built in memory onboard the cameras.

3.2. Experimental series performed with NMC and LFP cells

Experiments were performed with two different, similarly-sized, commercially available rechargeable cells under the three abuse modes. The two cell types being tested were an LG 18650 (model MG1, part LGDBMG11865) and a K2 26650 (model LFP26650P). The 26650 cell format describes a maximum 26.5 mm diameter and 65.4 mm long cell. The 18650 cell format describes a maximum

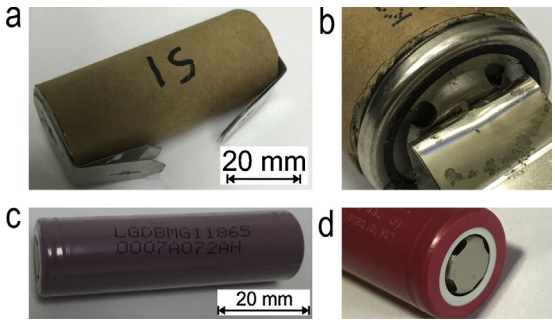

Fig. 3. An example of the tested (a) LFP cells before testing with (b) an additional view of the exposed vents. For comparison, an image of the chosen (c) NMC cell and (d) a view of the vents.

18.6 mm diameter and 65.2 mm long cell. Images of these cells with scale references are seen in Fig. 3(a) and (c). These cells are specifically chosen as they represent similar form factors common in mobile systems such as consumer electronics and electric vehicles, yet they represent two fundamentally different chemistries. The LG 18650 cell is a NMC while the K2 26650 is a LFP. Manufacturer specifications of both cells are included in Table 1 which demonstrates that the test series described in Section 3.1 is beyond the rated capabilities of these cells.

Custom fixtures for each cell were designed for rigid mounting of the cell and cartridge heaters on appropriate tests. All battery fixtures were electrically isolated from the test chamber. The LFP cells were purchased in a tabbed version, then 6.5 mm holes were drilled in each to allow for connection to the overcharge circuit via a screw connection to a crimped lug on 6 AWG wire. Tabbed connection was chosen as to have a minimal impact on venting flow patterns. Stainless steel hose clamps were used to hold the cell and cartridge heaters to a Tee-shaped aluminum plate. The NMC was not tabbed and thus a commercially available holder with built-in electrical connections was used. The vents on the NMC cells are unobstructed, but shortly after exiting the cell any gases vented downward impinge on the holder. The gases vented vertically propagate into the open space of the chamber. The flow patterns observed in the vertical venting are assumed to be representative of all vent exhausts if there was no holder present.

The holder was reinforced with a laser-cut 6 mm thick acrylic plate with bolt holes allowing for firm connection of the overcharge circuit. Hose clamps were used to hold cartridge heaters against the cell when needed. The surface temperature thermocouple was fixed centrally to the upper portion of all cells with aluminum foil tape.

In all of the experiments performed the batteries started from an approximately full charge state, and the time axis on all plots represents the duration of the test. The exact initial charge state between cells may vary slightly so no detailed analysis of the times to failure are presented.

Repeatability of test facility operation was confirmed with initial tests on the K2 26650 cells in an overcharge scenario of 11 A. The test durations are determined by the time from initiation of charging until current measurement indicates the battery acting as an open loop. On the three repeated tests of K2 26650 cells, durations range from 856.5 s to 873.2 s. This correlated to additional charging of cells between 2.62 Ah and 2.67 Ah. As seen in Fig. 4, voltage measurements in all tests follow a similar charging trend before failure and similar times to failure, showing that the process is generally repeatable and the data acquisition is consistent.

4. Experimental results

4.1. Battery venting observations

In all tests performed within the comparative series between the NMC and LFP cells, electrical failure and some form of venting were observed. These two failures generally coincided with one another. Venting was noted as the release of material internal to the cells from the designed vents in the cell cases, which for both of these cells were located under the positive terminal. Table 2 summarizes the qualitative observations of venting in each abuse condition. Representative images from each abuse condition are presented in Fig. 5. While venting was observed in all six tests, no "jelly-roll" ejection from the outer cell case was observed which has been previously demonstrated in literature [18]. In tests where liquid venting occurred, liquid would vent concurrently with gases but would stop being vented before gases stopped venting. Combination tests in both cells were more vigorous based on the presence of more vented gas and smoke. The NMC cells failures frequently resulted in combustion of the vented materials within the test chamber. The source of the ignition was not identified here, only the observed combustion possibility is reported.

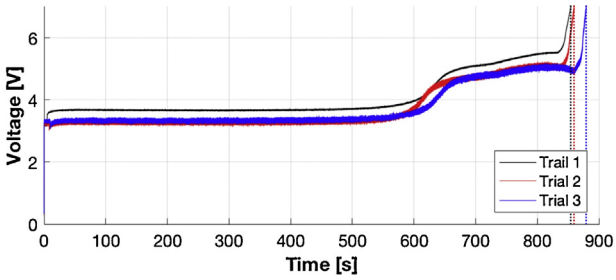

Fig. 4. Voltage trends before failure for three K2 26650 cells subjected to overcharge at 11 A before failure. Dashed vertical lines represent the moment when electrical failure of the battery is noted.

Venting flow from both the NMC and LFP cells followed similar general trends as both the 18650 and 26650 cell formats have radially located vents on the positive end of the cell. The 18650 cells have vents located under the terminal, and the 26650 cells have vents around the terminal underneath a paper overwrap which is crimped into place. The vents are shown in Fig. 3(b) and (d). All venting produced a flow projected radially outwards and slightly away from the end of the cell as seen in Fig. 6 for side and axis views. A minority of the venting would flow nearly axial with the length of the cell.

While the venting flow was generally consistent, the initial opening of battery vents appeared variable in rate and geometry. From the series performed with the LFP cells, axial schlieren images from 1 ms after initial venting are seen in Fig. 7. The relative rates of the vented material flow can be attributed to the vigor of the failure. Pressure build up within the cell cases leading to opening of the radially located vents should ideally produce consistent opening patterns. From the images shown, individual trials can have venting onset focused in different directions. While there are a finite number of vent holes on each battery, apparent bias in venting onset direction is greater than what should be expected from differing battery orientation within the fixture. The trials taken in this series show that there is variability of vent opening patterns before becoming fully open, but more trials would need to be performed to quantify any trends.

An experimental observation during failure tests of both the NMC and LFP cells is the presence of smoke within the test chamber. As summarized in Table 2, the presence of smoke in the venting process is more likely with the LFP cells and in tests where external heating is present. Increased smoke generation could be related to the decomposition products of the LFP chemistry of these cells versus the NMC system in the LG 18650 cell. However, direct comparison cannot necessarily be made between the two

Table 1
Specifications of NMC [16] and LFP [17] cells used in comparative testing.

	LG MG1	K2 LFP26650P
Chemistry	NMC	LFP
Format	18650	26650
Standard charging voltage	4.2 V	3.65 V
Capacity at C/5 discharge rate	2.85 Ah	2.60 Ah
Maximum charging voltage	4.2 V	4.1 V
Maximum charge rate	2.85 A	5 A

Table 2
Observed venting characteristics.

Cell	Overcharge 10 A	Thermal 75 W	Combination 10 A/75 W
LFP	Liquids and gases	Gases and smoke	Solids, gases, and smoke
NMC	Liquids and gases	Gases, liquids, and solids	Solids, smoke, and combustion

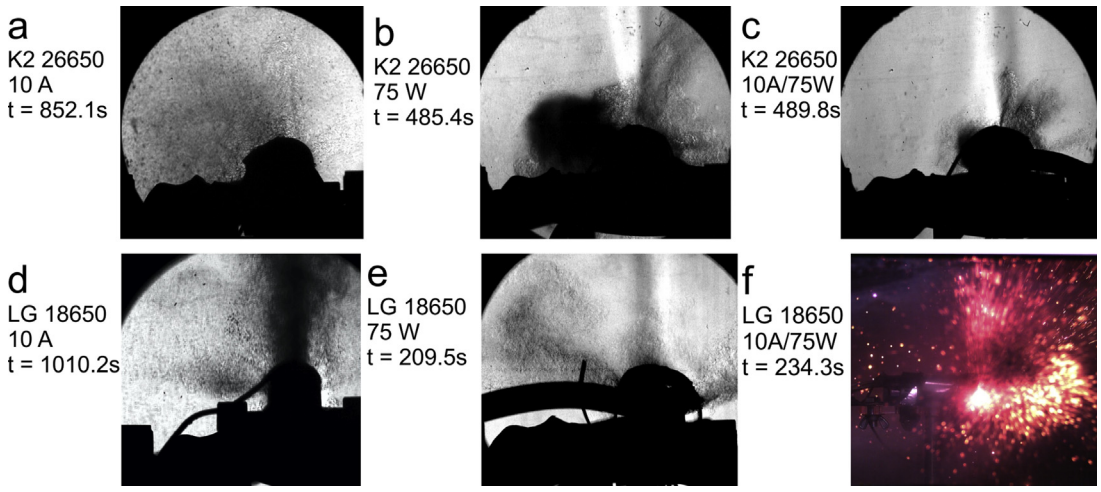

Fig. 5. (a–e) Still frames from high speed schlieren and (f) color video from tests in experimental series with LFP (K2 26650) and NMC (LG 18650) cells. Times listed represent the time of the frame from the beginning of the test. These frames represent initial venting of batteries before viewing became obscured by electrolyte liquids impacting the window or smoke filling the test chamber. Smoke can be seen left of the cell in image (b).

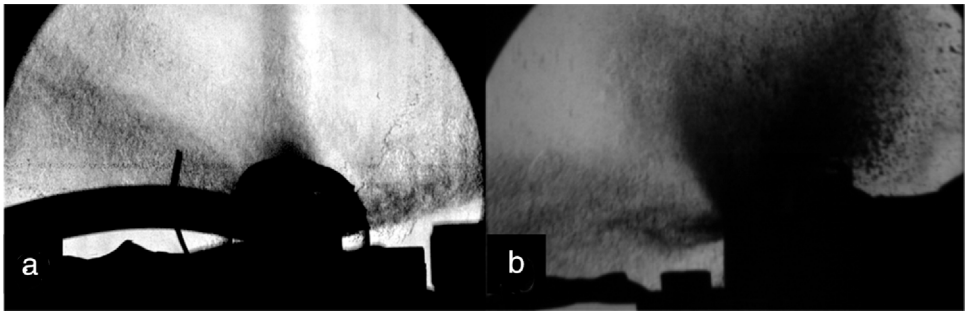

Fig. 6. (a) Axial and (b) side views of schlieren imaging during the NMC thermal failure test. Both images represent the venting pattern 1.85 ms after first visual failure of the cell.

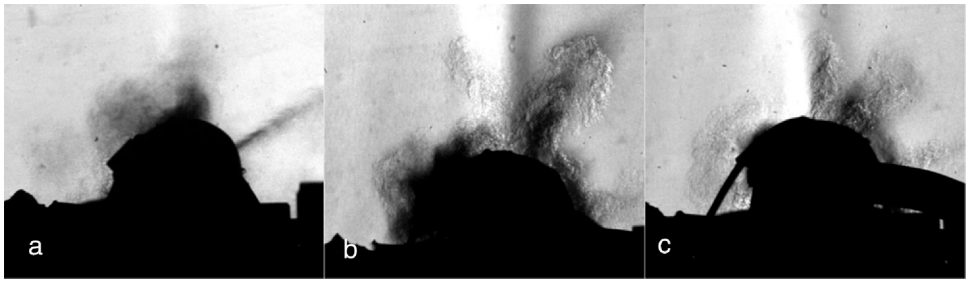

Fig. 7. Axial schlieren images of the LFP series of tests 1 ms after initial venting. These images show how opening patterns of vents can be variable between tests. Images are from (a) overcharge, (b) thermal, and (c) combination tests.

cell chemistries in terms of the amount of smoke generated from this test series. The smoke generation is likely proportional to the amount of electrolyte in each cell, which varies between the two battery geometries and chemistries.

4.2. Electrical trends between different failure modes

Electrical failure of the cells is observed in two primary modes: the battery being unable to accept further charge or when battery voltage decreases significantly to nearly zero. In the overcharge

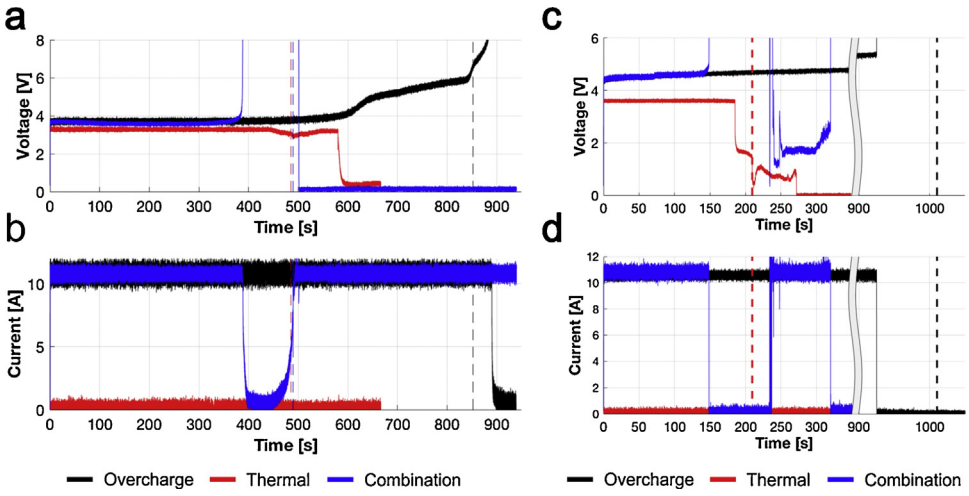

Fig. 8. (a) Voltage and (b) current traces for overcharge, thermal, and combination tests performed with LFP cells. (c) Voltage and (d) current traces for overcharge, thermal, and combination tests performed with NMC cells. The red, black, and blue dashed lines depict the onset of venting noted for the thermal, overcharge, and combination tests respectively. (For interpretation of the references to color in this figure legend, the reader is referred to the web version of this article.)

and combination tests where charging is present at a 10 A constant rate, a sudden drop in current to a zero value is indicative the battery acting as a break in the circuit ("open loop") most likely due to proper internal protective device activation or separator shutdown. For thermal heating tests where no current is present in the circuit, electrical failure is noted rather as the onset of the sharp drop in voltage. Electrical failure times for the 75 W thermal tests are measured at approximately 443 s and 185 s for the LFP and NMC cells respectively.

Current and voltage measurements were taken during all tests, and these traces follow specific trends which can be used to describe and possibly predict failure events. Fig. 8 shows these measurements versus time since test initiation for all three test types for the LFP and NMC cells. Additionally, these plots show when venting was first noted, when available, for the specific trials. Venting onset was not measured for the NMC combination test as the high speed video recording only included the second failure event which coincided with the reconnection at 234.9 s. For NMC measurements, the time axis is shortened and no deviations in the trends for the current or voltage in the overcharge tests were observed during the removed time portion. Samples are taken at 1 kHz while data represented has a moving average filter applied over a 10 ms width.

Comparing initial venting to the electrical characteristics of the cells provides for a close correlation. Table 3 below compares the time duration between initial venting and determined electrical failure. A negative number indicates venting before electrical failure while a positive number suggests the converse. The NMC combination trial high speed video did not include initial venting, so a time difference could not be reported.

The electrical failures on the two cell types are similar. Both cells charged with consistently increasing voltages until an open loop state occurred. This was also the case for the combination tests with the additional presence of a *reconnection* and acceptance of more charge. The thermal tests both show a level voltage until the point of electrical failure. While both battery types reached zero voltage measured in the thermal tests, the NMC had a more rapid decrease in voltage after electrical failure.

Table 3
Time between venting onset and electrical failure.

Cell	Overcharge 10 A	Thermal 75 W	Combination 10 A/75 W
LFP	−38.0 s	42.5 s	101.0 s
NMC	84.8 s	24.2 s	Not measured

4.3. Reconnection phenomena during thermal-overcharge tests

Combination thermal-overcharge tests show a high likelihood of more hazardous battery failures under both cell chemistries than either the thermal or overcharge tests alone which is related closely to the observed reconnection phenomena due to an internal short circuit. The reconnection refers to when the battery begins accepting charge again after going open loop which is seen on the current versus time plots in Fig. 8(b) and (d). Potentially, this could be attributed to melting of the separator within the cell providing an internal short circuit condition.

In the LFP test, the initial venting happened at the moment of reconnection. This failure was noted by rapid venting of solids, gases, and smoke as well as pressure waves seen in axial schlieren images. Onset of venting occurred at 489.8 s while reconnection is noted at 489.7 s after initiation of the test. The minimal time difference between venting and reconnection shows a strong correlation between the two events.

The NMC experienced a secondary failure at the moment of reconnection even though the battery was already venting. This secondary failure of the NMC battery displayed the only combustion event observed during the comparative test series. Combustion during this test momentarily spread across the entirety of the test chamber internal volume. The high speed video frame immediately after this moment is seen in Fig. 5(f). The relation between the combustion event and reconnection was seen in the air temperature measurement. The air temperature had a step increase at the same time as reconnection. This temperature peak does not add quantitative understanding though because the time response of the thermocouple is similar to the duration of combustion within the chamber. Additionally, the secondary failure of the cell caused significant damage to the cell and mounting fixture including melting of the ABS and acrylic plastic components.

4.4. Pressure wave propagation

The thermal and combination tests with the LFP cells show the presence of pressure waves in the axial view immediately

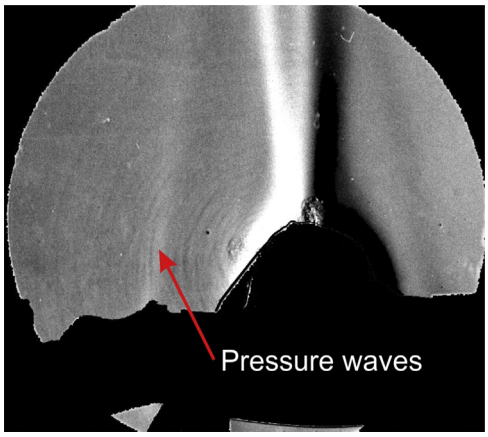

Fig. 9. Digitally processed image to highlight the pressure waves visible in the axial schlieren immediately after initial venting. Pressure waves are annotated by the arrow in the image. The frame shown is 0.1 ms after initial venting.

after venting. This can be seen in Fig. 9 showing the thermal test at a time 0.1 ms after failure. Pressure waves can be seen as the darkened concentric circular features most visible to the left of the cell in the image. These features within the schlieren images are indicative of finite air density changes across individual waves. This density change is not quantified, but its presence implies that these pressure waves are approximately sonic [19]. As the series waves does not coalesce, the resulting temperature difference and therefore sound speed increase across each wave is minimal. This observation implies that the shock waves are very weak, approximately Mach 1 shock waves. The high rate of gas venting associated with these abuse conditions allows inference of high enough internal pressures in the battery to have a sonic condition at the vent plane. This directly leads to the generation of compressible flow features. External shock waves present a risk in battery applications as they could be damaging to adjacent batteries potentially triggering another failure.

No conclusive evidence was found of pressure waves in other tests because schlieren imaging was often obstructed by smoke or combustion on most energetic failures and thermal shock on the piezoelectric pressure transducer rendered quantification of dynamic pressure peaks unreliable. While tests with the NMC cells, such as the 10 A/75 W combination test, appeared more energetic and likely to create a strong shock wave, these instrumentation limitations made analysis inconclusive.

5. Conclusions

A laboratory facility was constructed to test batteries of various chemistries and form factors under overcharge, thermal, and combination abuse conditions. High speed imaging was performed alongside more common measurements such as current, voltage, and temperature. Schlieren imaging allowed imaging of vented gases and pressure waves alongside liquid and solid material. While the presence of violent failures with lithium batteries is well known, schlieren images of pressure waves at initial failure provide insight into the venting process.

A comparative series between K2 26650 (LFP) and LG 18650 (NMC) cells provides results on the failures of the different batteries under 10 A overcharge, 75 W thermal, and 10 A/75 W combination abuse tests. Observations of the material vented during failures were made, including qualitative assessment of venting during initial failure and later-time steady-state venting. Based on the relative vigor of the reactions and demonstrated capability for combustion, the inherent risks of NMC are demonstrated.

Thermal-overcharge combination tests showed the most violent failures of both battery types. These significant energetic failures are correlated with a reconnection phenomena. This documented occurrence is when a cell which has already stopped charging and acted as an open-loop begins accepting more current suddenly due to an internal short circuit within the cell. After reconnection the observed venting became more significant and resulted in more material being ejected and combustion events within the battery chamber in some instances. These tests provide a link to possible worst-case scenarios for batteries in use as overcharge and heating could potentially exist simultaneously.

Measurements taken during all tests in this facility were able to be correlated via time which provides a more complete understanding of the conditions surrounding electrical and physical cell failure. Incorporation of high-speed optical techniques allows for applicable and novel understanding the venting process.

Acknowledgements

This work was funded by the Office of Naval Research under contract N00014-15-1-2265. Special thanks to Dr. David Wetz, Associate Professor of Electrical Engineering at UT Arlington, for loaning the power supplies used here.

References

[1] C. Kang, Galaxy Note 7 Owners Are Urged to Stop Using Their Phones, New York Times, 2016 9 September, http://www.nytimes.com/2016/09/10/technology/samsung-galaxy-consumer-product-safety.html.
[2] U. Irfan, How Lithium Ion Batteries Grounded the Dreamliner: Official report on Boeing 787 fires tells a cautionary tale about advanced batteries, Scientific American, 2014 18 December, https://www.scientificamerican.com/article/how-lithium-ion-batteries-grounded-the-dreamliner/.
[3] NASA Engineering and Safety Center Technical Bulletin No. 09-02 (2009).
[4] P.G. Balakrishnan, R. Ramesh, T. Prem Kumar, Safety mechanisms in lithium-ion batteries, J. Power Sources 155 (2006) 401–414, doi:http://dx.doi.org/10.1016/j.jpowsour.2005.12.002.
[5] S.S. Zhang, Insight into the gassing problem of Li-ion battery, Front. Energy Res. 2 (2014) 1–4, doi:http://dx.doi.org/10.3389/fenrg.2014.00059.
[6] Q. Wang, P. Ping, X. Zhao, G. Chu, J. Sun, C. Chen, Thermal runaway caused fire and explosion of lithium ion battery, J. Power Sources 208 (2012) 210–224, doi:http://dx.doi.org/10.1016/j.jpowsour.2012.02.038.
[7] H. Huang, T. Faulkner, J. Barker, M.Y. Saidi, Lithium metal phosphates power and automotive applications, J. Power Sources 189 (2009) 748–751, doi:http://dx.doi.org/10.1016/j.jpowsour.2008.08.024.
[8] A.W. Golubkov, D. Fuchs, J. Wagner, H. Wiltsche, C. Stangl, G. Fauler, G. Voitic, A. Thaler, V. Hacker, Thermal-runaway experiments on consumer Li-ion batteries with metal-oxide and olivin-type cathodes, RSC Adv. 4 (2013) 3633–3642, doi:http://dx.doi.org/10.1039/C3RA45748F.
[9] B.L. Ellis, W.R.M. Makahnouk, Y. Makimura, K. Toghill, L.F. Nazar, A multifunctional 3.5 V iron-based phosphate cathode for rechargeable batteries, Nat. Mater. 6 (2007) 749–753, doi:http://dx.doi.org/10.1038/nmat2007.
[10] P.T. Coman, S. Rayman, R.E. White, A lumped model of venting during thermal runaway in a cylindrical Lithium Cobalt Oxide lithium-ion cell, J. Power Sources 307 (2016) 56–62, doi:http://dx.doi.org/10.1016/j.jpowsour.2015.12.088.
[11] W.C. Chen, J.D. Li, C.M. Shu, Y.W. Wang, Effects of thermal hazard on 18650 lithium-ion battery under different states of charge, J. Therm. Anal. Calorim. 121 (2015) 525–531, doi:http://dx.doi.org/10.1007/s10973-015-4672-3.
[12] Y. Fu, S. Lu, K. Li, C. Liu, X. Cheng, H. Zhang, An experimental study on burning behaviors of 18650 lithium ion batteries using a cone calorimeter, J. Power Sources 273 (2015) 216–222, doi:http://dx.doi.org/10.1016/j.jpowsour.2014.09.039.
[13] D.P. Finegan, M. Scheel, J.B. Robinson, B. Tjaden, I. Hunt, T.J. Mason, J. Millichamp, M. DiMichiel, G.J. Offer, G. Hinds, D.J.L. Brett, P.R. Shearing, In-operando high-speed tomography of lithium-ion batteries during thermal runaway, Nat. Commun. 6 (6924) (2015) 1–10, doi:http://dx.doi.org/10.1038/ncomms7924.
[14] G.S. Settles, Schlieren and Shadowgraph Techniques: Visualizing Phenomena in Transparent Media, Springer, Berlin, 2001.
[15] M.J. Hargather, G.S. Settles, M.J. Madalis, Schlieren imaging of loud sounds and weak shock waves in air near the limit of visibility, Shock Waves (2009) 1–9, doi:http://dx.doi.org/10.1007/s00193-009-0226-6.

[16] LG Chem, Rechargeable Lithium Ion Battery Model: INR 18650 MG1 2850Ah, datasheet, 11 December 2014. [Rev. 3] https://www.imrbatteries.com/content/lg_MG1.pdf.
[17] K2 Energy, High Capacity LFP26650P Power Cell Data, datasheet. [Rev. SP-7000.80-002/A] http://liionbms.com/pdf/k2/LFP26650P.pdf.
[18] R.E. Lyon, R.N. Walters, Energetics of lithium ion battery failure, J. Hazard. Mater. 318 (2016) 164–172, doi:http://dx.doi.org/10.1016/j.jhazmat.2016.06.047.
[19] J.E.A. John, T.G. Keith, Gas Dynamics, Pearson, Upper Saddle River, NJ, 2006.